Received: 12 March 2020 | Revised: 14 May 2020 | Accepted: 15 May 2020

DOI: 10.1111/jace.17269

Journal of the American Ceramic Society

ORIGINAL ARTICLE

Model for the cold sintering of lead zirconate titanate ceramic composites

Dixiong Wang | **Kosuke Tsuji** | **Clive A. Randall** | **Susan Trolier-McKinstry**

Department of Materials Science and Engineering, The Pennsylvania State University, University Park State College, PA, USA

Correspondence
Dixiong Wang, Department of Materials Science and Engineering and the Materials Research Institute, The Pennsylvania State University, University Park State College, PA 16802, USA.
Email: dow5263@psu.edu

Funding information
National Science Foundation, Grant/Award Number: EEC-1160483

Abstract

A model was developed to describe the cold sintering process (CSP) of lead zirconate titanate (PZT) using moistened lead nitrate as a sintering aid. The densities of PZT powder with different volume fractions of lead nitrate were evaluated after cold sintering at 300°C and 500 MPa for 3 hours. The densities were categorized into three zones. In zone I, the relative density following cold sintering increases from 66% to 80%, as the lead nitrate contents rise from 0 to 14 vol%. In this case, the lead nitrate acts to fill some of the pore volume between PZT grains. Zone II serves as a transition region, where there is both pore filling and dilution of the PZT grains associated with lead nitrate contents from 14 to 34 vol%. In zone III, the relative density drops due to dilution at lead nitrate contents exceeding 34 vol%. To slow the process down so that the kinetics could be studied more readily, samples were cold sintered at room-temperature and 500 MPa. It was found that during the first few seconds of compaction, 85PZT/15Pb$(NO_3)_2$ rapidly densified from 51% to 61% relative density due to particle re-arrangement. For longer times at pressure, the CSP improved the packing relative to PZT compacted without the lead nitrate, yielding a higher relative density. The late stages of the PZT/Pb$(NO_3)_2$ CSP could be well described using a viscous sintering model for pressures from 50 MPa to 1000 MPa and temperatures from 25°C to 300°C.

KEYWORDS

cold sintering, lead zirconate titanate, low temperature, sinter/sintering

1 | INTRODUCTION

Of the various energy-efficient sintering techniques, the cold sintering process (CSP) holds the most potential for ultra-low temperature sintering. Although most of the CSP papers have been published within the past 5 years, the origin of this technique may be traced back to the 1800s for metals[1,2] and 1950-1960s when researchers started to realize the presence of moisture increased the green density in oxides and sulfates which reduced the sintering temperatures.[1,3,4] In the 1970-1980s, the word "cold sintering" was first used to refer to a process utilizing "plastic deformation of powder particles in a high pressure gradient at ambient temperature resulting in green densities close to theoretical" for metals, glass, and ionic crystals.[5] At the same time, the hydrothermal hot-pressing (HHP) method was proposed for the densification of cement materials at low temperatures.[6,7] Kähäri et al showed Li_2MoO_4 (LMO) could be sintered at near room temperatures by adding water and higher uniaxial pressures, noting that large particles are beneficial for the densification.[8,9] The group at Penn State University outlined the path toward a universal strategy for the cold sintering process in which particles were mixed with a small amounts of solvent (often aqueous or polar organics). This enabled controlled

dissolution at low temperatures and applied pressures; subsequently, the solvent is evaporated from the open system.[10] In many cold sintering studies, ceramic pellets can be sintered to >95% relative density at <300°C.[8,9,11] In short, densification under such low temperatures is realized by introducing uniaxial pressures in conjunction with transient phases that (often) partially dissolve the ceramics, re-arrange the particle compact, and re-precipitate the dissolved ions at the pores when the liquid phase is vaporized. Thus, the sintering mechanism of CSP seems to be similar to that of liquid phase sintering (LPS)[12,13] or pressure solution creep (PSC).[14-16] Research on CSP was quickly adopted with hundreds of publications and patents on the CSP of oxides,[11,17-21] inorganic salts,[22-25] and composites[26-30] covering applications including high frequency antennas,[30,31] energy storage capacitors,[32,33] battery components,[22,24,25] varistors,[11,26] and piezoelectric sensors/actuators.[18,34] Cold sintering of inorganic-inorganic composites was achieved by mixing low solubility ceramics with high solubility salts or oxides, such as Al_2SiO_5/NaCl,[35] PZT/$Pb(NO_3)_2$,[18] and PZT/Li_2MoO_4.[34] In such cases, it is conjectured that the soluble phases lubricate the insoluble ceramics, resulting in improved compaction. From this perspective, the sintering mechanism in the composite is expected to be very different from that in the single-phase case. This hypothesis has not been proved, neither has the underlying mechanism been explained.

Therefore in this work, based on the early report on cold sintering PZT with moistened $Pb(NO_3)_2$ at 300°C, 500 MPa for 3 hours, the effects of experimental parameters including lead nitrate volume fraction, temperature, pressure, and holding time were explored. A physical model is proposed to describe the late stages of the CSP of such inorganic-organic composites.

2 | EXPERIMENTAL PROCEDURE

PZT powders with a bimodal size distribution (medium particle sizes of 50 nm and 600 nm) were used for the study of $Pb(NO_3)_2$ content, temperature, pressure, and holding time. The powder was produced by attrition milling (Szegvari Attritor System Type B Model 01-HD, Union Process, Inc) commercial PZT-5A powder (PKI-509, PiezoKinetics Inc) for 12 hours. The particle size analysis was measured using a laser diffractometer (Mastersize 3000, Malvern Analytical Ltd.), and checked by a scanning electron microscope (Verios G4, FEI).

To avoid pressure fluctuations, a hydraulic press with a pressure stabilizing regulator, similar to that designed by Floyd et al,[36] was utilized for the CSP. This pressure regulator uses a spring-loaded nozzle to constrain oil flow and stabilize pressure, allowing independent control of temperature and pressure. For each PZT pellet, different mass ratios of raw PZT powder and $Pb(NO_3)_2$ powder (Sigma-Aldrich Corp.) were mixed and ground while the total weights have been controlled to be 0.77 g. 0.5 mL deionized water was added to the mixture to dissolve the lead nitrate. The mixture was then ground in a mortar and pestle until the water was mostly vaporized, removing the soft agglomerates in PZT. After grinding, the mixture was loaded into a cylindrical die (Wartburg Tool & Die, Wartburg, TN) and pressed at 25°C-300°C, under 50-1000 MPa for 15-180 minutes. The pellets cold sintered at <100°C were dried in open air for over 24 hours to remove residual water that might affect the measured sintered density. The densities of the pellets were measured by the geometrical method. The final dimensions of the cold sintered pellets are half-inch-diameter (~12.77 mm) with thicknesses between 0.8 and 1.1 mm.

A self-built dilatometer using a contact distance sensor (Keyence GT2-H32, Itasca, IL) attached to the press was used to monitor the linear shrinkage of PZT pellet during the pressing at room temperature.[36] Because most of the shrinkage from compaction happens in the first 5 minutes, the data time interval was set to 0.1 second for the first 5 minutes, and 3 seconds for the rest of the process. In order to accurately reflect the thickness change of only the pellet, a calibration run was first carried out with an empty cylindrical die at the same temperature, pressure, and time interval setup, in order to determine the background curve. Then the background was subtracted from the actual measured profiles during pressing to get the sample thickness vs pressing time profiles ($L(t)$). The thickness profiles ($L(t)$) were converted to relative density profiles ($\rho_{rel}(t)$) using measured sample masses (m), pellet top surface areas (A), and the theoretical density ($\rho_{theoretical}$) of either 85PZT/15$Pb(NO_3)_2$ (=7.32 g/cm^3) or PZT (=7.8 g/cm^3) according to the following equation:

$$\rho_{rel}(t) = \frac{m/(A \cdot L(t))}{\rho_{theoretical}} \quad (1)$$

The PZT volume fraction of 85PZT/15$Pb(NO_3)_2$ can be calculated by multiplying 0.85 times $\rho_{rel}(t)$, while the relative density of the dry pressed PZT equals to its volume fraction.

3 | RESULTS AND DISCUSSION

The size distribution of the attrition-milled PZT-5A powder is plotted in Figure 1A. The peaks above 3 μm reflect soft agglomerates in the powder, as was corroborated by the SEM in Figure 1B. Those soft agglomerates were believed to be eliminated by the high shear grinding procedure in a mortar and pestle prior to the cold sintering process.

Should the densification of PZT powder during the CSP be attributable to the lubrication associated with the lead nitrate solution under pressure and temperature, the effect of the

lead nitrate volume fraction in the system should be obvious. Because there is negligible dissolution of PZT in the transient liquid phase during the CSP, the as-cold sintered pellet can be considered to be a composite of PZT, $Pb(NO_3)_2$, and air (pores). For the purposes of the model, the possibility of partial decomposition of lead nitrate was ignored for simplicity; this should be a reasonable approximation because the weight loss from nitrogen dioxide is much less than that of the remaining lead oxide, as reported previously.[18] Therefore, the lead nitrate serves to densify the PZT at low volume fraction while "diluting" the PZT at high volume fraction. Experimentally, this trend is described in Figure 2.

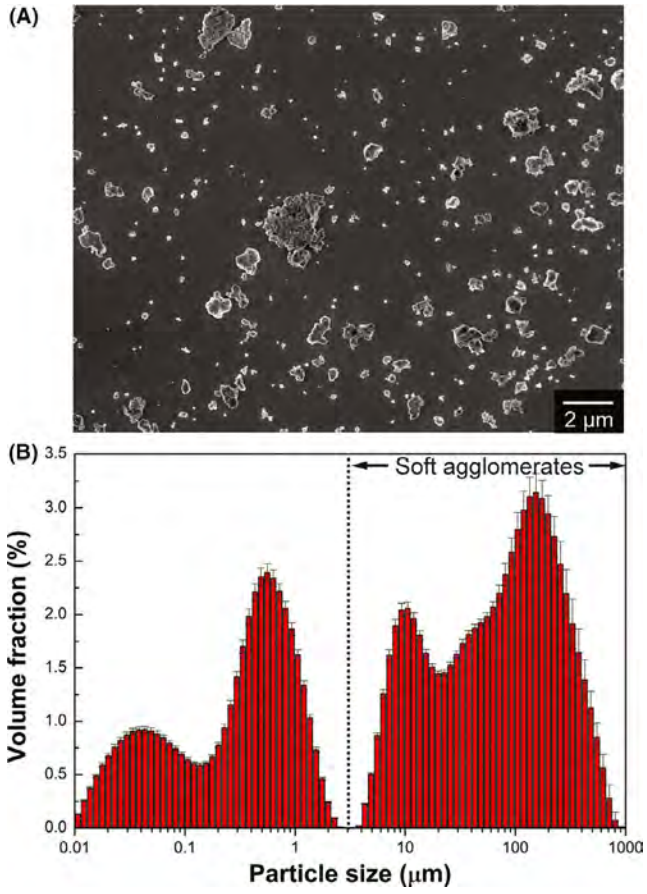

FIGURE 1 A, The size distribution measured via laser diffractometer and (B) the SEM image of the attrition-milled PZT-5A powder [Color figure can be viewed at wileyonlinelibrary.com]

Figure 2 was constructed using ρ_{PZT} = 7.80 g/cm^3, $\rho_{Pb(NO_3)_2}$ = 4.53 g/cm^3, ρ_{total} from the geometrical measurements, and the calculated $\rho_{theoretical}$ based on the composite composition. The porosity curve is a function of the lead nitrate volume fraction as described by Equation 2.

$$\text{Porosity} = V_{\text{pore}}^{\text{relative}} = 1 - \frac{\rho_{\text{total}}}{\rho_{\text{theoretical}}} = 1 - \frac{\rho_{\text{total}}}{\rho_{PZT} \cdot \frac{V_{PZT}^{\text{relative}}}{V_{PZT}^{\text{relative}} + V_{Pb(NO_3)_2}^{\text{relative}}} + \rho_{Pb(NO_3)_2} \cdot \frac{V_{Pb(NO_3)_2}^{\text{relative}}}{V_{PZT}^{\text{relative}} + V_{Pb(NO_3)_2}^{\text{relative}}}} \quad (2)$$

where ρ_{total} is the real density of the pellet, and $V^{relative}$ is the volume fraction of the constituent in the composite. From the same equation, a relationship between the PZT volume fraction and lead nitrate volume fraction can be acquired, assuming $\frac{V_{PZT}^{relative}}{V_{Pb(NO_3)_2}^{relative}}$ is constant before and after the CSP (ie that the composition is constant during cold sintering).

A second relationship between PZT volume fraction ($V_{PZT}^{relative}$) and lead nitrate volume fraction ($V_{Pb(NO_3)_2}^{relative}$) is given by the experimentally measured densities (Equation 3), in which m is the mass.

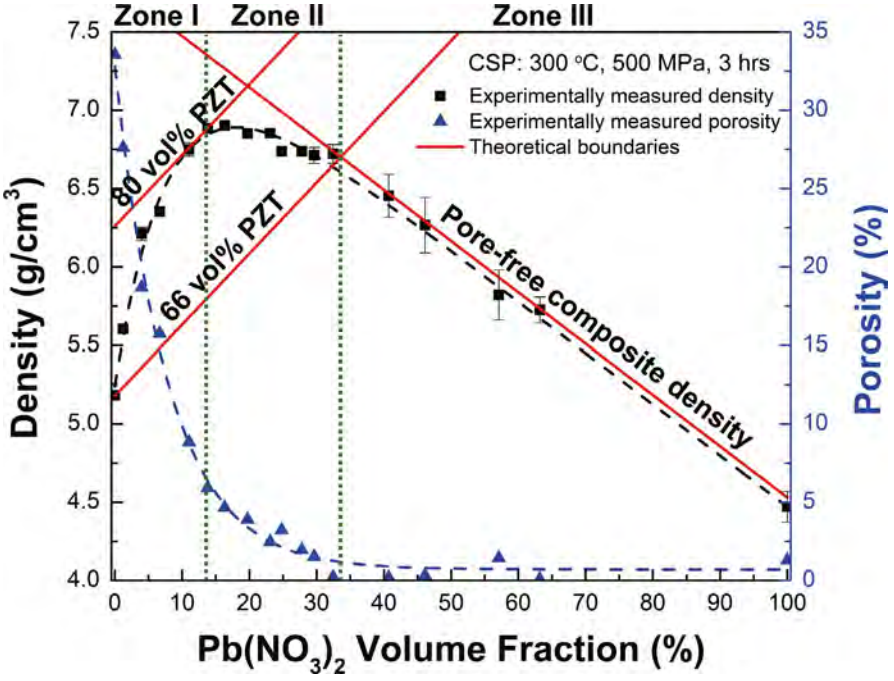

FIGURE 2 Density (black) and Porosity (blue) evolution of PZT/$Pb(NO_3)_2$ with respect to $Pb(NO_3)_2$ volume fraction. The chart was divided into 3 zones based on the densification of PZT and the reduction of porosity. The red lines represent the theoretical density boundaries [Color figure can be viewed at wileyonlinelibrary.com]

$$\rho_{\text{total}} = \frac{m_{\text{total}}}{V_{\text{total}}} = \frac{m_{\text{PZT}} + m_{\text{Pb(NO}_3)_2}}{V_{\text{PZT}} + V_{\text{Pb(NO}_3)_2} + V_{\text{pore}}} = \frac{\rho_{\text{PZT}} V_{\text{PZT}} + \rho_{\text{Pb(NO}_3)_2} V_{\text{Pb(NO}_3)_2}}{V_{\text{PZT}} + V_{\text{Pb(NO}_3)_2} + V_{\text{pore}}} = \frac{\rho_{\text{PZT}} V_{\text{PZT}}^{\text{relative}} + \rho_{\text{Pb(NO}_3)_2} V_{\text{Pb(NO}_3)_2}^{\text{relative}}}{V_{\text{PZT}}^{\text{relative}} + V_{\text{Pb(NO}_3)_2}^{\text{relative}} + V_{\text{pore}}^{\text{relative}}} \quad (3)$$

When all the known values as well as the calculated porosities are plugged into Equation 3, the PZT volume fraction and the lead nitrate volume fraction can be calculated.

As can be seen from Figure 2, the densities of the pellets increase with $Pb(NO_3)_2$ content until the volume fraction of the lead nitrate reaches 16 vol%; this is accompanied by a rapid decrease in porosity. Then, pellet densities drop because the PZT particles are diluted by the lead nitrate. It should be noted that the PZT packing densities are slightly offset from the pellet densities. This occurs because the pellet densities represent the composite densities of PZT and $Pb(NO_3)_2$, while the PZT packing densities only focus on the PZT volume fraction in the pellets. Although the PZT powder shows improved relative packing densities from 66% to 80% when there is 0-14 vol% lead nitrate, more lead nitrate starts to reduce the PZT volume fraction in the composite while continuing filling of the pores. As a result, when the lead nitrate volume fractions increase from 14 vol% to 34 vol%, the relative packing density of PZT drops from 80 vol% to 66 vol%. In summary, the contributions of lead nitrate to the cold sintered pellet can be briefly divided into three zones:

Zone I: $Pb(NO_3)_2$ lubricates and densifies PZT while helping fill the pores.

Zone II: Transition region in which $Pb(NO_3)_2$ keeps filling the pores but also starts to dilute the PZT.

Zone III: $Pb(NO_3)_2$ has finished filling most of the pores, and acts primarily to dilute the PZT.

Experimental data have shown that the pellet densities rise with elevated cold sintering temperatures and/or cold sintering pressures. This is shown in Figure 3A,B. Here, a theoretical density of 7.32 g/cm^3 was used as a reference, corresponding to a composite of 85 vol% PZT and 15 vol% $Pb(NO_3)_2$.

The liquid phase sintering models used to describe cold sintering of ZnO[37,38] are not applicable here due to the lack of a PZT dissolution-precipitation process. Therefore, a different model that illustrates the contributions of temperature and pressure during the CSP of PZT is necessary. This was attempted by assuming that the lead nitrate experiences plastic deformation under uniaxial pressure. The resulting "pseudo viscous flow" is temperature dependent due to the thermal activation of the viscosity. Under this assumption, the widely used equation from Murray et al[3] for viscous sintering can be adopted as a starting point.

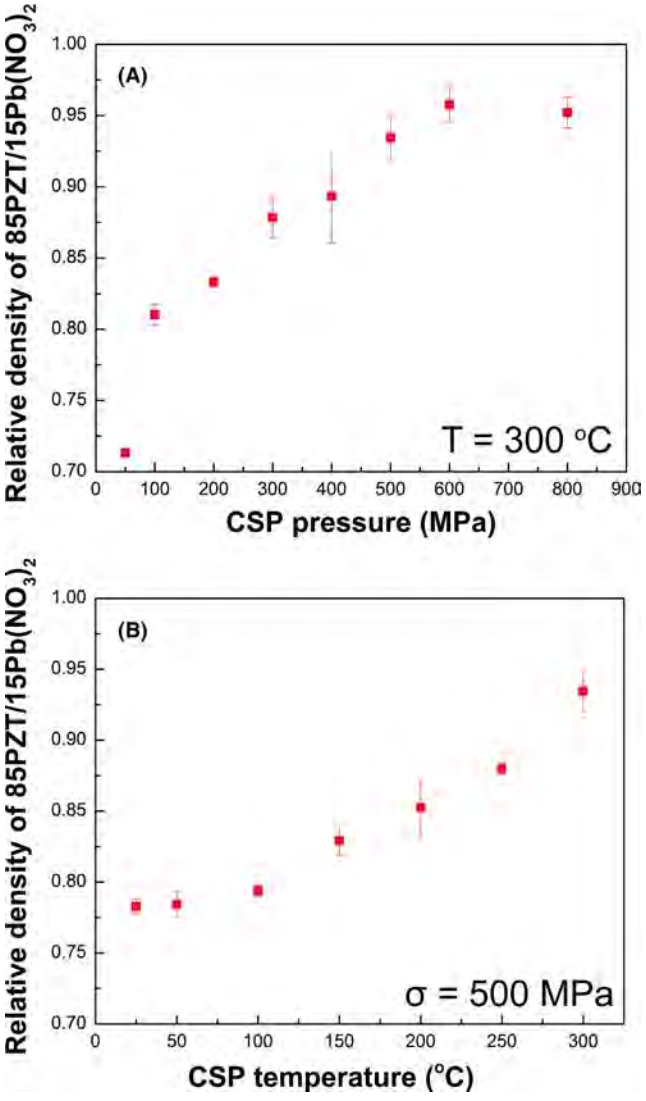

FIGURE 3 Relative densities of 85 vol% PZT and 15 vol% $Pb(NO_3)_2$ composite after cold sintering at (A) different uniaxial pressures (at 300°C) and (B) different temperatures (under 500 MPa). A theoretical density of 7.32 g/cm^3 was used as a reference [Color figure can be viewed at wileyonlinelibrary.com]

The original equation developed by Murray et al have the form:

$$\rho = 1 - e^{-\left(\frac{3\sigma}{4\eta}\right)t+c} \quad (4)$$

where ρ is relative density, σ is the applied uniaxial pressure in MPa, η is the viscosity of the material, t is the sintering time in minute, and c is a constant. This equation describes the relationship between relative density and pressure, but an explicit temperature term is missing. This can be rectified using the Vogel-Fulcher-Tammann (VFT)[39] equation for the temperature dependence of the viscosity:

$$\eta = \eta_0 e^{\frac{b}{T-T_0}} \quad (5)$$

here η is the viscosity, T is temperature in °C, b, and T_0 are constants.

By substituting Equation 5 into Equation 4, Equation 6 can be derived. This equation directly relates the relative density, temperature, pressure, and time:

$$\rho = 1 - e^{-\left(\frac{3t}{4\eta_0}\right)\sigma e^{-b/(T-T_0)}+c} \quad (6)$$

With some re-arrangement, the following two forms occur:

$$\ln(1-\rho) = -\left(\frac{3t}{4\eta_0}\right) e^{-b/(T-T_0)}\sigma + c \quad (7)$$

$$\ln(-\ln(1-\rho)+c) = \ln\left(\frac{3t\sigma}{4\eta_0}\right) - \frac{b}{T-T_0} \quad (8)$$

Equations 7 and 8 imply that there is a linear relationship between *ln(1-ρ)* and pressure, and a hyperbolic relationship between *ln(-ln(1-ρ)+c)* and temperature.

Figure 4A shows the experimental data plotted as for Equation 7. Fitting the 300°C data in Figure 4A gives Equation 9 for uniaxial pressure in MPa:

$$\ln(1-\rho)_{T=300°C} = (-0.00254 \pm 0.000313)\,\sigma - 1.30 \pm 0.138 \quad (9)$$

Using c = −1.30 in Equation 9, Figure 4B can be plotted and Eq. 8 can be parameterized as Equation 10:

$$\ln(-\ln(1-\rho)+c) = (-4.21 \pm 1.79) - \frac{1790 \pm 1890}{T - 696 \pm 274} \quad (10)$$

These fits give R^2 of 0.94 for the density-pressure relationship and 0.98 for the density-temperature relationship, suggesting the later stages of the cold sintering of PZT can be reasonably described as a viscous-sintering-related process.

It is notable that the fitting in Equation 10 indicates large confidence limits for b and T_0. This is most likely because the curve shape from the VFT model is insensitive to b and T_0 changes in this temperature range. Thus, an alternative fitting strategy is to apply the Arrhenius relationship (Equation 11), resulting in two linear relationships (Equations 12 and 13):

$$\eta = \eta_0 e^{-b'T} \quad (11)$$

$$\ln(1-\rho) = -\left(\frac{3t}{4\eta_0}\right) e^{b'T}\sigma + c \quad (12)$$

$$\ln(-\ln(1-\rho)+c) = \ln\left(\frac{3t\sigma}{4\eta_0}\right) + b'T \quad (13)$$

where *b'* is another constant.

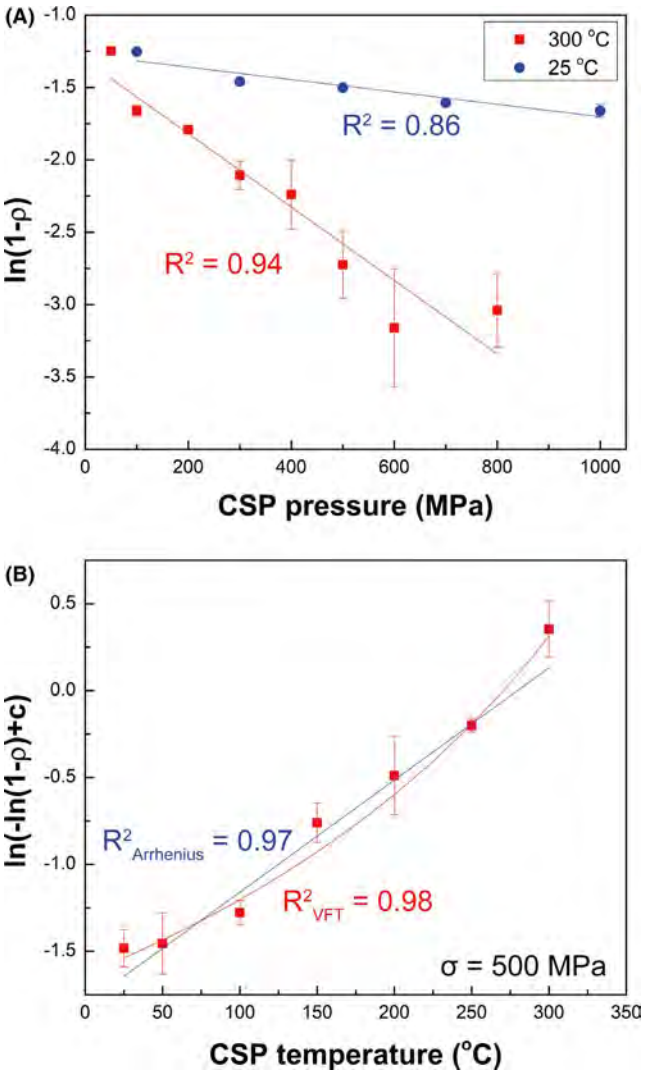

FIGURE 4 Experimental data in Figure 3A,B is replotted in the forms of (A) Equation 7 and (B) Equation 8/Equation 13, respectively. Relative densities vs. uniaxial pressures acquired at room temperature are shown by a blue curve in (A) [Color figure can be viewed at wileyonlinelibrary.com]

As seen in Figure 4, the fit for the *ln(1-ρ)* - pressure plot is not affected by choice of either an Arrhenius or VFT model for the viscosity. It was found that the *ln(-ln(1-ρ)+c)*—temperature fit also resulted in a good R^2 (97%) with fitting parameters shown in Equation 14:

$$\ln(-\ln(1-\rho)+c) = (-1.79 \pm 0.0936) + (0.00670 \pm 0.00044)\,T \quad (14)$$

The viscous sintering model may also be applied to predict and optimize cold sintering conditions. For example, from Equation 9, by assuming constant t, η_o, b (b'), T_0 and c, the *ln(1-ρ)*—pressure relation can be predicted for 25°C, giving the following equations from the VFT model (Equation 15) and Arrhenius model (Equation 16), respectively:

$$\ln(1-\rho)_{\mathrm{VFT},T=25°C} = -0.000398\sigma - 1.30 \quad (15)$$

$$\ln(1-\rho)_{\text{Arrhenius},T=25^{\circ}\text{C}} = -0.000402\sigma - 1.30 \quad (16)$$

Again, the uniaxial pressure is in MPa.

From experimental data for cold sintering at 25°C, Eq. 17 was determined from Figure 4A:

$$\ln(1-\rho)_{T=25^{\circ}\text{C}} = -0.000415 \pm 0.0000834\sigma - 1.27 \pm 0.0506 \quad (17)$$

The similarity in slopes and intercepts of Equation 15, Equation 16, and Equation 17 suggests that the viscous sintering model is capturing the essential physics of the behavior for samples at the end of the cold sintering process.

In addition, according to Equation 12, the sintering time should present a linear relationship with *ln(1-ρ)*. This portion of the hypothesis, however, could not be proven experimentally at 300°C. Figure 5A depicts the pellet relative densities with respect to CSP time at 300°C. The schematic temperature profile indicates the heating system requires ~17 minutes to reach 300°C and ~20 minutes to cool to below 60°C (a temperature low enough to unload the sample safely) while the porosity dropped to <10% during the heating and cooling procedures.

To better characterize the effect of time on the density of the pellet, both standard pressing dry PZT powder without lead nitrate and PZT with lead nitrate/water experiments were carried out at 25°C. Using the dilatometer on the press, the thickness shrinkage of the sample was determined. The resulting calculated relative density curves are shown in Figure 5B. It is apparent that the densification behavior of the PZT/$Pb(NO_3)_2$ alters in the first 800 seconds (~13 minutes). The density curve suggests the densification of the composite most likely experiences 3 stages: The first stage happens in the initial two seconds, and is characterized by the rapid increase in relative density. This is possibly caused by the rearrangement of PZT powder in the pressing die; it is probable that in this stage, the lead nitrate has not undergone extensive plastic deformation yet. This stage should happen regardless of the presence of lead

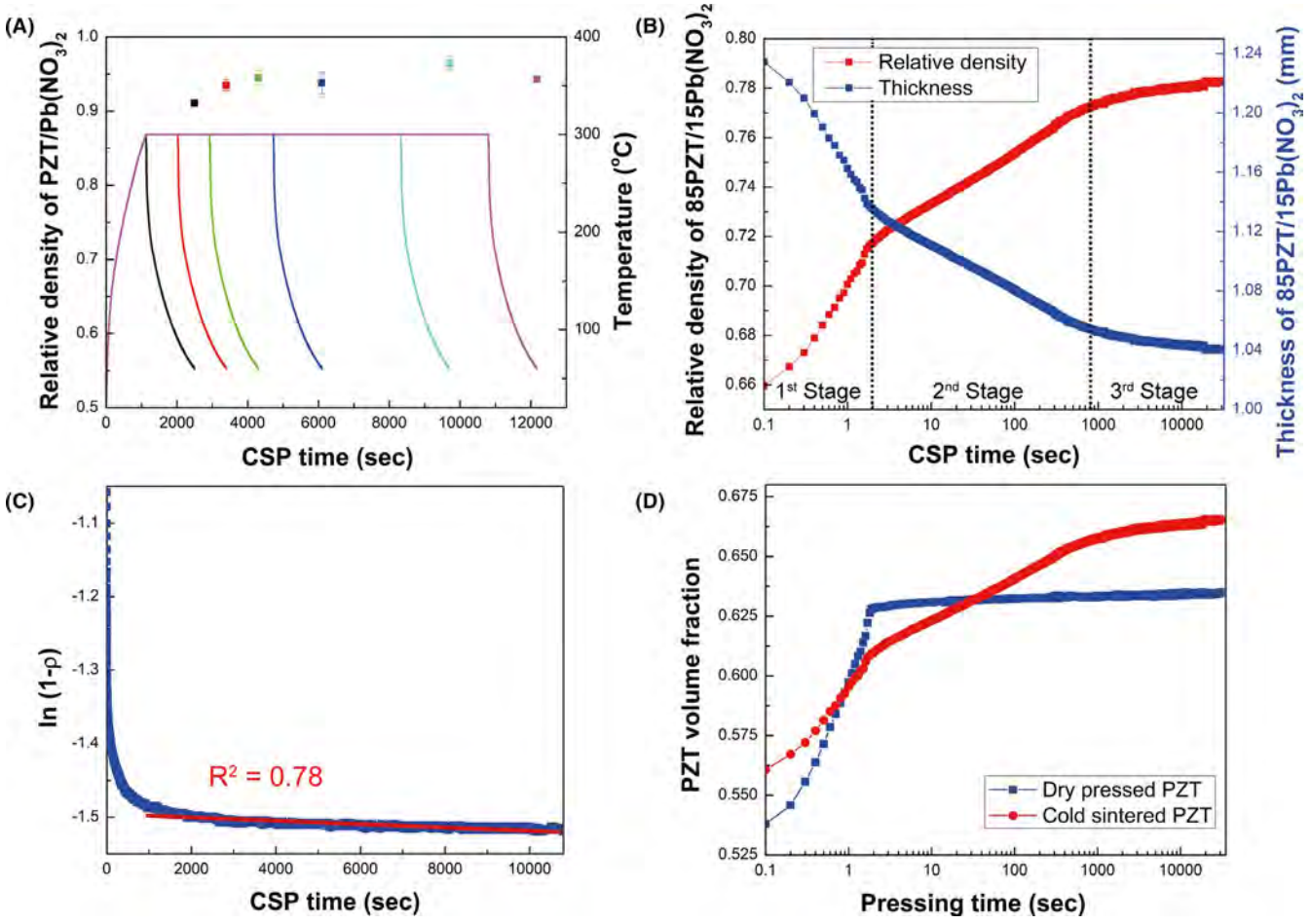

FIGURE 5 A, The relative densities of 85PZT/15Pb$(NO_3)_2$ after being cold sintered at different durations under 500 MPa at 300°C with temperature profiles shown as colored lines. (B) The thickness shrinkage and the corresponding density evolution of 25°C cold sintered 85PZT/15Pb$(NO_3)_2$ measured by the dilatometry on the uniaxial press. (C) A replot of the density curve in (B) in the form of Equation 12 with a linear fit (red line) of the 3rd stage of densification profile. (D) A comparison of the PZT volume fraction evolution in cold sintered pellet and dry pressed pellet [Color figure can be viewed at wileyonlinelibrary.com]

nitrate but can only reach a modest packing density. The fact that samples without the lead nitrate additive show a comparable rapid densification in the first several seconds is consistent with this observation.

The second stage takes place from ~2 to ~800 seconds, during which the densification of the cold sintered composite slows down. Because the dry-pressed part does not show nearly as much compaction in this time interval as the cold sintered parts, it is hypothesized that the curve in this period might be related to a combination of viscous sintering and water evaporation. Specifically, the lead nitrate starts to deform under pressure and moisture, enabling the further optimization of PZT compaction; while the water escapes from the die, the re-precipitation of lead nitrate causes a decrease in volume. After 16 minutes of cold sintering at room temperature, the rearrangement of PZT becomes significantly retarded as the packing is close to its geometrical limit. The $ln(1-\rho)$ vs time curve is also obtained by replotting the Figure 5B in the form of Equation 12, and is displayed as Figure 5C. It is obvious that the modified viscous sintering equation failed to describe, at least for the first 16 minutes, that $ln(1-\rho)$ is linearly related to the cold sintering time at room temperature, presumably because the cold sintering process is complicated by the initial particle rearrangement and water volatilization. Also, unlike the density-time relationship depicted in Figure 5A from the unloaded samples, the dilatometry profiles are measured in-situ. Since the data cannot capture the loading and unloading responses (due to tremendous noise from friction or vibration between die and plunges), the loading and unloading may have also affected the conditions of the samples. In stage 3 of the CSP (after 13 minutes), the curve presents a more linear shape and the fitting R^2 returns to 78% (Figure 5C), suggesting the densification mechanism might start to be dominated by Equation 12.

In comparing the compaction of the cold sintered and dry pressed PZT powders, it is clear that both systems experience rapid packing in the first 2 seconds. However, while the dry pressed sample displays almost no densification over the next couple of hours, the density of the cold sintered sample continues to increase, which corroborates the hypothesis that the moisturized lead nitrate can further optimize the packing of the particles. Interestingly, at the end of the first stage, the PZT volume fraction of the dry pressed sample is a little higher than the cold sintered sample. This is possibly because the addition of moisturized lead nitrate will hinder the rapid particle rearrangement by increasing the spacing between PZT particles. After ~800 seconds, viscous sintering of the lead nitrate takes over and eventually leads to a higher density in the cold sintered parts.

Finally, it is notable that although not focused on composite systems, a recent publication by Haug et al. on cold sintering agglomerated nanovaterite demonstrated a linear relationship between $1/\rho \cdot d\rho/dt$ and σ, which, after integration, is similar to the logarithmic relationship between uniaxial pressure and the relative densities found in this work[40] This suggests the plastic deformation may be extensively present when cold sintering materials that consist mainly of insoluble powders. However, the mechanical creep with respect to time in dry/wet nanovaterite system differs from that within dry/wet PZT/$Pb(NO_3)_2$ composites, in that the densification of wet nanovaterite pellets is constantly faster and more complete than in dry pellets,[41] while in PZT/$Pb(NO_3)_2$ systems the wet composite densifies slower than the dry one in the first 2 seconds. This indicates a possible viscosity difference between pure water and wet lead nitrate as a sintering aid, which suggests that the specific details of the process need to be treated on a case-by-case basis. Other low temperature sintering models, such as the hydrothermal sintering models for ZnO,[37,38] the reactive hydrothermal sintering model for $BaTiO_3$,[42] and the plastic deformation model for NaCl,[23] targeted rather dissimilar systems where the powders participate in the typical "dissolution-reprecipitation" process, and are expected to behave differently. In contrast, in this work, Zr^{4+} and Ti^{4+} in PZT have very limited solubility in water, and the additional Pb^{2+} from $Pb(NO_3)_2$ would suppress potential leaching of lead from PZT.[43]

4 | CONCLUSIONS

PZT ceramic composites were cold sintered to >80% relative densities at 300°C using bimodal PZT powder with moistened $Pb(NO_3)_2$ as a sintering aid. The underlying mechanism of PZT densification during cold sintering is improved PZT particle packing induced by the plastic deformation of the moist lead nitrate phase; this is a new method by which cold sintering can be performed. Therefore, a viscous sintering model can be utilized to explain the effects of temperature, pressure, and time on the final pellet densities in the third stage of the cold sintering process; the model showed good agreement with experimental results in terms of pressure and temperature. For the first two stages, particle rearrangement and moisture evaporation also affect the densification as a function of time.

ACKNOWLEDGMENTS

This research is supported by the National Science Foundation (NSF) Advanced Self-Powered Systems of Integrated Sensors and Technologies (ASSIST) (Grant Number: EEC-1160483). The authors thank the Center for Dielectrics and Piezoelectrics (CDP) for the help. The authors also appreciate support from Richard Floyd and Jon-Paul Maria for sharing the design of their hydraulic press, and Tim Klinger for helping assemble the hydraulic press.

ORCID

Dixiong Wang https://orcid.org/0000-0002-2067-3646
Kosuke Tsuji https://orcid.org/0000-0001-9346-4450
Clive A. Randall https://orcid.org/0000-0002-5478-2699
Susan Trolier-McKinstry https://orcid.org/0000-0002-7267-9281

REFERENCES

1. Grasso S, Biesuz M, Zoli L, Taveri G, Duff AI, Ke D, et al. A review of cold sintering processes. Adv Appl Ceram. 2020;119(3):115–43.
2. Kendall K. Theoretical aspects of solid-solid adhesion. Sci Progress, Oxford. 1988;72(2):155–71.
3. Murray P, Rodgers EP, Williams AE. Practical and theoretical aspects of hot pressing of refractory oxides. Trans Br Ceram Soc. 1954;53(8):474–510.
4. Turba E, Rumpf H. Zugfestigkeit von Preßlingen mit vorwiegender Bindung durch van der Waals-Kräfte und ihre Beeinflussung durch Adsorptionsschichten. Chemie Ing Tech. 1964;36(3):230–40.
5. Gutmanas EY, Lawley A. Cold Sinteirng - A new powder consolidation process. Prog Powder Metall. 1983;39:1–15.
6. Roy DM, Gouda GR, Bobrowsky A. Very high strength cement pastes prepared by hot pressing and other high pressure techniques. Cem Concr Res. 1972;2(3):349–66.
7. Yamasaki N, Yanagisawa K, Nishioka M, Kanahara S. A hydrothermal hot-pressing method: apparatus and application. J Mater Sci Lett. 1986;5:355–6.
8. Kahari H, Teirikangas M, Juuti J, Jantunen H. Dielectric properties of lithium molybdate ceramic fabricated at room temperature. J Am Ceram Soc. 2014;97(11):3378–9.
9. Guo H, Baker A, Guo J, Randall CA, Johnson D. Cold sintering process: a novel technique for low-temperature ceramic processing of ferroelectrics. J Am Ceram Soc. 2016;99(11):3489–507.
10. Randall CA, Guo J, Baker A, Lanagan M, Guo H. Cold sintering ceramics and composites. United States patent 2017/0088471 A1. 2017. https://patents.google.com/patent/US20170088471A1/en
11. Funahashi S, Guo J, Guo H, Wang KE, Baker AL, Shiratsuyu K, et al. Demonstration of the cold sintering process study for the densification and grain growth of ZnO ceramics. J Am Ceram Soc. 2017;100(2):546–53.
12. Kingery WD. Densification during sintering in the presence of a liquid phase. I. Theory. J Appl Phys. 1959;30(3):301–6.
13. Guo J, Floyd R, Lowum S, Maria J-P, Herisson de Beauvoir T, Seo J-H, et al. Cold sintering: progress, challenges, and future opportunities. Annu Rev Mater Res. 2019;49(1):275–95.
14. Gratier JP, Guiguet IR. Experimental pressure solution-deposition on quartz grains: the crucial effect of the nature of the fluid. J Struct Geol. 1986;8(8):845–56.
15. Bouville F, Studart AR. Geologically-inspired strong bulk ceramics made with water at room temperature. Nat Commun. 2017;8:14655.
16. Bang SH, Ndayishimiye A, Randall CA. Anisothermal densification kinetics of the cold sintering process below 150°C. J Mater Chem C. 2020;8(17):5668–72.
17. Guo H, Bayer TJM, Guo J, Baker A, Randall CA. Cold sintering process for 8 mol%Y_2O_3-stabilized ZrO_2 ceramics. J Eur Ceram Soc. 2017;37(5):2303–8.
18. Wang D, Guo H, Morandi CS, Randall CA, Trolier-McKinstry S. Cold sintering and electrical characterization of lead zirconate titanate piezoelectric ceramics. APL Mater. 2018;6(1):016101.
19. Liu J-A, Li C-H, Shan J-J, Wu J-M, Gui R-F, Shi Y-S. Preparation of high-density $InGaZnO_4$ target by the assistance of cold sintering. Mater Sci Semicond Process. 2018;84:17–23.
20. Huang HQ, Tang J, Liu J. Preparation of $Na_{0.5}Bi_{0.5}TiO_3$ ceramics by hydrothermal-assisted cold sintering. Ceram Int. 2019;45(6):6753–8.
21. Ma J, Li H, Wang H, Lin C, Wu X, Lin T, et al. Composition, microstructure and electrical properties of $K_{0.5}Na_{0.5}NbO_3$ ceramics fabricated by cold sintering assisted sintering. J Eur Ceram Soc. 2019;39(4):986–93.
22. Lee W, Lyon CK, Seo J-H, Lopez-Hallman R, Leng Y, Wang C-Y, et al. Ceramic–salt composite electrolytes from cold sintering. Adv Funct Mater. 2019;29(20):1–8.
23. Hong WB, Li L, Cao M, Chen XM. Plastic deformation and effects of water in room-temperature cold sintering of NaCl microwave dielectric ceramics. J Am Ceram Soc. 2018;101(9):4038–43.
24. Seo J-H, Guo J, Guo H, Verlinde K, Heidary DSB, Rajagopalan R, et al. Cold sintering of a Li-ion cathode: $LiFePO_4$-composite with high volumetric capacity. Ceram Int. 2017;43(17):15370–4.
25. Pereira da Silva JG, Bram M, Laptev AM, Gonzalez-Julian J, Ma Q, Tietz F, et al. Sintering of a sodium-based NASICON electrolyte: a comparative study between cold, field assisted and conventional sintering methods. J Eur Ceram Soc. 2019;39(8):2697–702.
26. Zhao X, Guo J, Wang K, Herisson De Beauvoir T, Li B, Randall CA. Introducing a ZnO–PTFE (polymer) nanocomposite varistor via the cold sintering process. Adv Eng Mater. 2018;20(7):1–8.
27. Zhao Y, Berbano SS, Gao L, Wang KE, Guo J, Tsuji K, et al. Cold-sintered V_2O_5-PEDOT:PSS nanocomposites for negative temperature coefficient materials. J Eur Ceram Soc. 2019;39(4):1257–62.
28. Guo J, Legum B, Anasori B, Wang KE, Lelyukh P, Gogotsi Y, et al. Cold sintered ceramic nanocomposites of 2D MXene and zinc oxide. Adv Mater. 2018;30(32):1–6.
29. Wang D, Zhou D, Zhang S, Vardaxoglou Y, Whittow WG, Cadman D, et al. Cold-sintered temperature stable $Na_{0.5}Bi_{0.5}MoO_4$–Li_2MoO_4 microwave composite ceramics. ACS Sustain Chem Eng. 2018;6:2438–44.
30. Faouri SS, Mostaed A, Dean JS, Wang D, Sinclair DC, Zhang S, et al. High quality factor cold sintered Li_2MoO_4–$BaFe_{12}O_{19}$ composites for microwave applications. Acta Mater. 2019;166:202–7.
31. Kähäri H, Ramachandran P, Juuti J, Jantunen H. Room-temperature densified Li_2MoO_4 ceramic patch antenna and the effect of humidity. Int J Appl Ceram Technol. 2017;14:50–5.
32. Wang D, Zhou D, Song K, Feteira A, Randall CA, Reaney IM. Cold-sintered C0G multilayer ceramic capacitors. Adv Electron Mater. 2019;5(7):1–5.
33. Ma JP, Chen XM, Ouyang WQ, Wang J, Li H, Fang JL. Microstructure, dielectric, and energy storage properties of $BaTiO_3$ ceramics prepared via cold sintering. Ceram Int. 2018;44(4):4436–41.
34. Nelo M, Siponkoski T, Kähäri H, Kordas K, Juuti J, Jantunen H. Upside-down composites: Fabricating piezoceramics at room temperature. J Eur Ceram Soc. 2019;39(11):3301–6.
35. Induja IJ, Sebastian MT. Microwave dielectric properties of mineral sillimanite obtained by conventional and cold sintering process. J Eur Ceram Soc. 2017;37(5):2143–7.
36. Floyd R, Lowum S, Maria J-P. Instrumentation for automated and quantitative low temperature compaction and sintering. Rev Sci Instrum. 2019;90(5):055104.

37. Kang X, Floyd R, Lowum S, Cabral M, Dickey E, Maria JP. Mechanism studies of hydrothermal cold sintering of zinc oxide at near room temperature. J Am Ceram Soc. 2019;102(8):4459–69.
38. Bang SH, Ndayishimiye A, Randall CA. Mechanistic approach to identify densification kinetics and mechanisms of zinc oxide cold sintering. SSRN Electron J. 2019; Available from: https://www.ssrn.com/abstract=3428070.
39. Mauro JC, Yue Y, Ellison AJ, Gupta PK, Allan DC. Viscosity of glass-forming liquids. Proc Natl Acad Sci. 2009;106(47):19780–4.
40. Haug M, Bouville F, Ruiz-Agudo C, Avaro J, Gebauer D, Studart AR. Cold densification and sintering of nanovaterite by pressing with water. J Eur Ceram Soc. 2020;40(3):893–900.
41. Haug M, Bouville F, Adrien J, Bonnin A, Maire E, Studart AR. Multiscale deformation processes during cold sintering of nanovaterite compacts. Acta Mater. 2020;189:266–73.
42. Vakifahmetoglu C, Anger JF, Atakan V, Quinn S, Gupta S, Li Q, et al. Reactive hydrothermal liquid-phase densification (rHLPD) of ceramics – A study of the $BaTiO_3$[TiO_2] composite system. J Am Ceram Soc. 2016;99(12):3893–901.
43. Bakarič T, Budič B, Malič B, Kuščer D. The influence of pH dependent ion leaching on the processing of lead-zirconate-titanate ceramics. J Eur Ceram Soc. 2015;35(8):2295–302.

How to cite this article: Wang D, Tsuji K, Randall CA, Trolier-McKinstry S. Model for the cold sintering of lead zirconate titanate ceramic composites. *J Am Ceram Soc*. 2020;103:4894–4902. https://doi.org/10.1111/jace.17269